Journal of Applied Physics ARTICLE scitation.org/journal/jap

A critical evaluation of Ag- and Ti-hyperdoped Si for Si-based infrared light detection

Cite as: J. Appl. Phys. **129**, 065701 (2021); doi: 10.1063/5.0035620
Submitted: 30 October 2020 · Accepted: 19 January 2021 ·
Published Online: 8 February 2021

S. Q. Lim,[1,a)] A. J. Akey,[2] E. Napolitani,[3] P. K. Chow,[4] J. M. Warrender,[4] and J. S. Williams[1]

AFFILIATIONS

[1]Research School of Physics, The Australian National University, Canberra, ACT 2601, Australia
[2]Center for Nanoscale Systems, Harvard University, Cambridge, Massachusetts 02138, USA
[3]Dipartimento di Fisica e Astronomia "Galileo Galilei," Universià di Padova, 35131 Padova, PD, Italy
[4]U.S. Army Combat Capabilities Development Command—Armament Center, Watervliet, New York 12189, USA

[a)]**Author to whom correspondence should be addressed:** qi.lim@anu.edu.au

ABSTRACT

Following recent successful demonstrations of enhanced infrared absorption in Au-hyperdoped Si, there has been strong interest in fabricating other metal-hyperdoped Si systems as a highly attractive approach for Si-based infrared photodetection. In this work, we address the somewhat contentious issue in the literature as to whether it is possible, using ion implantation and nanosecond pulsed-laser melting, to achieve hyperdoping of Si with Ag and Ti at concentrations exceeding that required to form an intermediate impurity band within the Si bandgap ($N_{IB} \sim 6 \times 10^{19}$ cm^{-3}). A wide range of characterization techniques were used to investigate these material systems, especially the quality of liquid-phase epitaxy, impurity concentration distribution both in depth and laterally, and impurity lattice location. Our results indicate that the high concentrations of opto-electrically active Ag or Ti in monocrystalline Si required to form an impurity band are not achieved. In particular, the usual behavior during rapid solidification is for near-complete surface segregation of the impurity, or for it to be trapped within a highly defective subsurface layer due to filamentary breakdown. Although our measurements showed that the maximum concentration of impurities outside metal-rich filaments is comparable to N_{IB} for both Ag and Ti, there is no preferential Ag or Ti lattice location after pulsed-laser melting anywhere in the material. Thus, the concentration of opto-electrically active Ag and Ti that can be homogeneously incorporated into Si is expected to be well below N_{IB}, leaving Au as the only viable impurity to date for achieving the required level of hyperdoping in Si.

I. INTRODUCTION

Developing Si-based optoelectronics with sensitivity in the near- to mid-infrared (N/MIR) has always been of great interest and will see widespread applications across fields involving telecommunications, imaging, and optical computing. Being Si-based means that existing Si manufacturing and processing technologies can be leveraged, making it economically and technologically attractive. However, infrared light absorption in Si is fundamentally limited by its bandgap ($E_g = 1.11$ eV), and thus Ge and III–V compound semiconductors are often used as alternatives for infrared light detection. However, these alternatives can be expensive, and their integration with Si-CMOS is an ongoing challenge.

It is possible to enhance the NIR and MIR absorption properties of Si through deep sub-bandgap states (or deep levels), which can be introduced either intrinsically (by defects such as di-vacancies and interstitial clusters) or extrinsically (by "doping" with transition metals). The former technique has already been demonstrated with Si self-implantation experiments, where implantation-related deep level defects introduced into the Si bandgap have enabled sub-bandgap light absorption.[1–3] On the other hand, extrinsic deep levels in Si can arise from transition metal impurities present in specific lattice site locations within Si (e.g., substitutional or interstitial).[4] Thus, greatly enhanced NIR absorption could in principle be achieved in Si by doping with extremely high soluble concentrations of transition metal impurities, provided that they are in an electrically active lattice configuration with a sufficiently large optical cross section. Impurities satisfying such conditions will be loosely defined as being "opto-electrically active" in Si.

In the last two decades, there has been increasing research effort into the fabrication and characterization of Si containing high concentrations of transition metal impurities.[5] In particular,

metal concentrations of the order of 1 at. % (or 10^{20} cm^{-3}) in Si were successfully fabricated from ion implantation/thin film deposition followed by nanosecond pulsed-laser melting (PLM).[6–12] If these metal atoms are opto-electrically active in the Si lattice, at these high concentrations, metal-induced deep levels in Si are no longer discrete and an impurity band(s) forms within the Si bandgap.[13] This leads to the delocalization of impurity band electrons (and thus possibly higher conductivity/carrier mobility[13,14]) and substantial broadband infrared light absorption.[9] Such materials are often referred to as supersaturated or hyperdoped Si; we adopt the latter nomenclature throughout this work (readers are referred to Ref. 15 for a detailed review on the topic of laser hyperdoping in Si). The nominal concentration required for the formation of an impurity band, N_{IB}, has been estimated to be around 6×10^{19} cm^{-3} for most metal impurities in Si.[13] Thus, for the purpose of our work, we will define successful metal-hyperdoping in Si (for optoelectronic applications or optical hyperdoping) as when the metal is incorporated at concentrations exceeding N_{IB}, *while simultaneously being in an opto-electrically active lattice configuration*. Note that in the literature, hyperdoping can simply refer to achieving concentrations far beyond the impurity's equilibrium solid solubility limit in Si, which is often well below N_{IB}.

Ti was one of the first metal candidates explored for optical hyperdoping in Si, and thus there is an extensive number of publications related to the fabrication and physical, optical, and electrical characterization of such Si–Ti systems.[6–8,16–18] In particular, as the Ti implantation dose increased, these implanted and PLM processed Si–Ti samples showed improved sub-bandgap absorption[16] and conductivity,[6,18] as well as evidence of carrier lifetime recovery.[19] Other metal impurities that have gained interest over the last decade include Au,[9,20] V,[21] Fe, Co, Zn, Ni,[22,23] and Ag,[24] and in some cases, NIR photodetectors were demonstrated with these materials.[8,9,24] Among these metal impurities, Au is the most promising hyperdoping candidate in terms of the quality of epitaxy following PLM, opto-electrically active substitutional Au content, sub-bandgap absorption, and photocurrent properties.[9,25,26] Ag, on the other hand, has only been studied using Ag deposition and femtosecond-PLM.[24] Although the optical and electrical properties of such Si–Ag materials show some promise, it is important to note that femtosecond-PLM is known to introduce surface microstructures that are highly non-reflective in the near-to-mid infrared.[27,28] There is no known literature on Si–Ag fabricated from implantation and nanosecond-PLM.

However, there has been some controversy in the literature as to whether such Si–Ti materials are truly hyperdoped such that $N_{Ti} > N_{IB}$.[29,30] Alternative interpretations to anomalies observed in their physical[29,31] and electrical[30] properties suggest that a Ti-impurity band does not form from standard fabrication procedures involving Ti implantation and PLM. In particular, under experimental conditions in which concentration-depth profiling data suggest a concentration of Ti close to or greater than N_{IB}, the Si–Ti layer is observed to be defective after PLM, in that subsurface stacking faults and filamentary breakdown were observed.[29,31] Atom probe tomography measurements show that the Ti concentration outside of these breakdown structures is below 1×10^{18} cm^{-3} everywhere.[31] Percolation conduction between breakdown structures was proposed as an alternative carrier transport mechanism, rather than the delocalization of electrons due to the formation of an impurity band, both similarly giving rise to a higher than expected material conductivity and the observed carrier lifetime recovery phenomena in Si–Ti.[6,18,30]

In this work, we seek to determine the suitability of Ag and Ti as deep level impurities for optical hyperdoping in Si. Ag was initially chosen because it has similar deep levels to Au in Si. Si–Ag is also surprisingly similar to Si–Ti in terms of its physical characteristics under PLM, as will become apparent later. Here, we provide a detailed physical analysis that includes the lattice configuration of the Ag and Ti atoms in Si, the quality of the Si crystallinity, and the impurity distributions, using a wide range of experimental techniques. By combining results from multiple techniques, we are able to obtain a comprehensive understanding of the material. We then compare our observations to those on Au-hyperdoped Si in the literature, the only Si-metal system that has been unequivocally shown to exhibit hyperdoping behavior such that $N_{Au} > N_{IB}$.

II. EXPERIMENT

Samples were prepared on n-type Czochralski-grown <100> Si (0.5–2 Ω cm). <100> Si was chosen due to its higher tolerance to amorphization from faster melt-front velocities.[32] The implantation parameters for Ag and Ti are summarized in Table I. The implant energies were chosen such that the peak ion range is around 50 nm from the surface. Samples were implanted at 77 K to ensure the formation of a continuous amorphous layer and tilted 7° off beam axis to minimize ion channelling effects. Samples were then annealed at 350 °C for 30 min to sharpen the amorphous–crystal interface near the implant tail. Note that 350 °C is insufficient to cause solid phase epitaxial recrystallization[33] and below the temperatures at which Ti reacts with amorphous Si to form silicides,[34] noting that Ag does not form stable silicides even at elevated temperatures.[4] Samples were then subjected to PLM in air with a single, spatially homogenized, 6 ns laser pulse using the third harmonic (355 nm) of a Nd:YAG laser (Ekspla) over a 3×3 mm^2 aperture. The nominal PLM fluence was varied between 0.45 and 1.40 J/cm^2 by adjusting the laser energy density using a variable attenuator. Melt durations were measured by time-resolved reflectivity (TRR) measurements using a 488 nm Ar^+ ion laser.[35,36] For a given laser energy density, the melt duration of pristine Si was used to calibrate the nominal fluence using one-dimensional heat flow simulations. Note that our implanted samples have slightly different optical and thermal properties to that of pristine Si, and thus the melt depth is not known accurately. For each PLM fluence, several areas on the implanted sample were irradiated to monitor the shot-to-shot variation in the melt duration. This allowed us to monitor the laser fluence stability and sample quality

TABLE I. Summary of the implantation parameters used in our experiment.

Impurity	Implant energies (keV)	Nominal implant doses (cm^{-2})
Ag	80	1×10^{15}, 3×10^{15}, 1×10^{16}
Ti	45	1.5×10^{15}, 3×10^{15}, 5×10^{15}

and select the appropriate samples for characterization (see Appendix A of the supplementary material for more details).

Rutherford backscattering spectroscopy with channelling analysis (RBS-C) was performed with 2.0 MeV $^4He^+$ ions to examine the quality of epitaxy and impurity distribution after PLM. Backscattered He^+ ion energies were measured with Si detectors placed at 102° and 110° with respect to the incident beam axis for Si–Ag and Si–Ti samples, respectively, and analyzed with a multichannel analyzer. These scattering geometries were chosen to maximize the subsurface depth resolution of Ag and Ti, while avoiding spectral overlap with the substrate Si signal at lower channels. RBS channelled and random spectra were collected by aligning the beam with the sample's <100> axial channel and tilting the sample 7° off this channelling axis, respectively. Depth scales were calculated using relevant equations[37] and the simulation software package, RUMP.[38] RBS angular scan profiles were obtained by collecting RBS spectra at various sample tilt angles between −3° and 3° about the axial direction. The resulting angular scan profiles were obtained by integrating the impurity and Si signals of each of these RBS spectra over the appropriate depth regions.[37]

Secondary ion mass spectrometry (SIMS) was performed using a CAMECA IMS-4f instrument with a 14.5 keV Cs^+ sputtering beam. The Ag and Ti concentration and depth scales were calibrated by assuming the nominal implant dose and by measuring the crater depths with a profilometer, respectively. Transmission electron microscopy (TEM) and atom probe tomography (APT) samples were prepared using a FEI Helios Nanolab focused ion beam (FIB) system. For TEM, a Pt protective layer was deposited onto a selected area on the sample before milling and further thinning with a Ga^+ beam. For APT, a 100 nm Si protective layer was first evaporated over the sample with an electron beam. FIB was then used to process the sample into an APT-compatible tip, followed by a final annular Ar-ion mill at 5 kV (Fishione NanoMill 1040 system) to further sharpen the tip. TEM images were then collected using a JEOL JEM-2100F instrument operating at 200 keV, while APT measurements were performed using a CAMECA LEAP 4000 HR instrument equipped with a 355 nm picosecond pulsed laser. In APT, samples were held at 40 K and a 40 pJ pulsed-laser (100 kHz repetition rate) was used to induce field evaporation of atoms at the apex of the sample tip. Subsequent APT data reconstruction and analysis were performed with the CAMECA IVAS software.

III. RESULTS

A. Si–Ag system

RBS-C revealed that two of our three Ag implanted samples solidified with good quality epitaxy after PLM. These are the 80 keV Ag 1×10^{15} cm^{-2} and 3×10^{15} cm^{-2} samples that received PLM fluences $\geq$0.70 and 1.10 J/cm^2, respectively. These fluences are necessary to melt beyond the amorphous–crystal interface and thus induce liquid-phase epitaxy on the underlying crystalline substrate. On the other hand, defective epitaxy was observed in the 80 keV Ag 1×10^{16} cm^{-2} sample even at PLM fluences as high as 1.40 J/cm^2 (beyond which surface ablation effects become significant). The representative RBS spectra for these samples are plotted in Figs. 1(a) and 1(b). To better understand these RBS spectra, we divide our analysis into two regions, separated by the gray vertical line at channel 370 shown in Fig. 1. The signal to the left arises from He^+ ions backscattered by Si substrate atoms, while to the right from Ag impurity atoms. The Si and Ag surface edges are represented by the 0 nm mark on the corresponding depth scales. Information about the quality of epitaxy following PLM can be obtained by comparing the Si backscatter yield of PLM samples to that of pristine Si under channelling conditions, while the Ag signal represents the concentration-depth distribution of Ag in Si (note that we do not calculate or show the Ag concentration axis in Fig. 1).

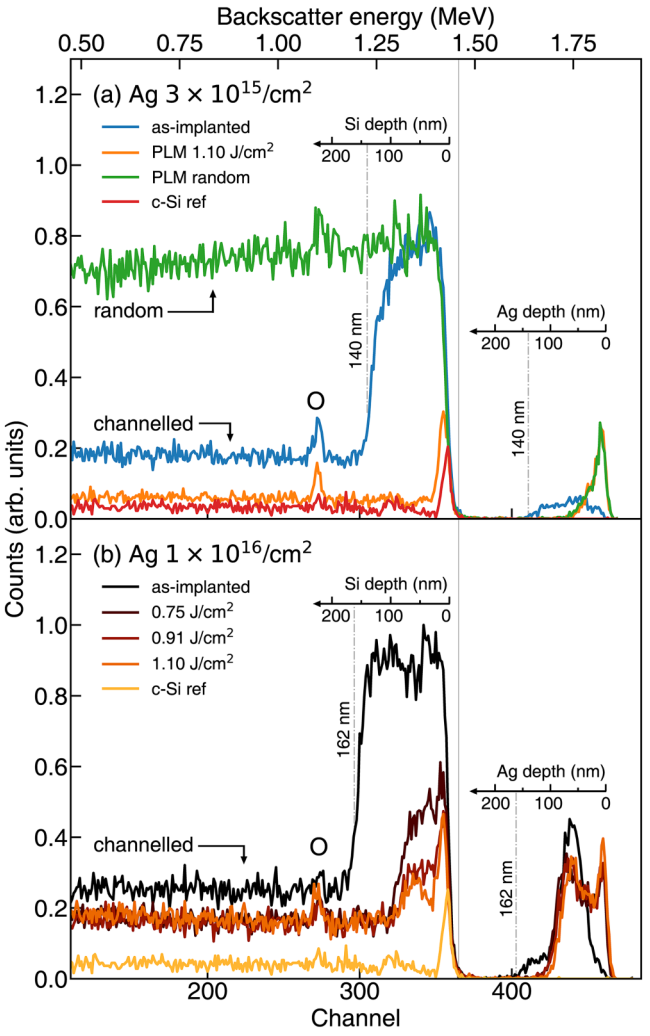

FIG. 1. RBS spectra for 80 keV Ag (a) 3×10^{15} cm^{-2} (PLM 1.10 J/cm^2) and (b) 1×10^{16} cm^{-2} samples PLM at different laser fluences, showing (a) good epitaxy, along with Ag surface segregation or; (b) defective epitaxy, following PLM. The as-implanted spectrum and a pristine Si reference spectrum (c-Si ref) are also shown to aid comparison.

Before examining the PLM samples, we first point out some important features present in both the as-implanted RBS spectra in Figs. 1(a) and 1(b). After implantation, a (continuous) amorphous layer was formed on the surface of the $3 \times 10^{15}\,\mathrm{cm}^{-2}$ and $1 \times 10^{16}\,\mathrm{cm}^{-2}$ Ag samples, measuring 140 ± 5 nm and 162 ± 5 nm in thickness, respectively. The corresponding as-implanted Ag signals were also observed to terminate at these depths. Note that there is a small shoulder feature toward the deeper end of the Ag signal (between channels 400 and 425). This is due to some Ag diffusion in amorphous Si during the 350 °C pre-anneal performed before PLM. It is well known that low temperature annealing causes impurities with high diffusivities in Si (such as Ag) to diffuse throughout the amorphous layer.[39,40] Thus, the Ag atoms in our as-implanted samples have diffused all the way up to the crystalline–amorphous interface during pre-annealing at 350 °C.

After PLM, the channelled RBS spectrum in Fig. 1(a) showed a low Si backscattering yield behind the Si surface peak that is similar to that of pristine Si (c-Si ref), indicative of good epitaxy. On the other hand, practically all of the Ag implanted atoms have segregated to the surface (at least as determined within the detection capability of RBS, $\sim 10^{19}\,\mathrm{cm}^{-3}$ for Ag). Surface segregation is indicated by the prominent Ag surface peak at channel 460. This was observed in both the channelled and random spectra. Furthermore, the channelled and random Ag signals are identical, suggesting that there is no substitutional Ag or other preferred atom location site within the Si lattice, within the sensitivity of RBS. There is also a long Ag tail that extends further into the substrate (down to 50 nm), which will be discussed later and also in Appendix B in the supplementary material. The surface oxide has thickened in both the as-implanted and PLM samples (relative to the pristine Si native oxide), represented by an O peak at channel 270.

As for the 80 keV Ag $1 \times 10^{16}\,\mathrm{cm}^{-2}$ sample, we plot in Fig. 1(b) a collection of RBS spectra for this sample at various PLM fluences. The broad Si features between channels 320 and 360 and the high backscatter yields at lower channels indicate defective epitaxy following PLM. This subsurface defective spectrum yield decreases in amplitude with increasing PLM fluence, while maintaining a constant width (thickness) of approximately 80 nm. The RBS spectrum for the same sample subjected to PLM at $1.40\,\mathrm{J/cm}^2$ was identical to that at $1.10\,\mathrm{J/cm}^2$ shown in Fig. 1(b) and thus not plotted for clarity. As for the Ag signal, we observed significant quantities of Ag trapped within the defective layer in addition to surface segregation. The subsurface and surface Ag peaks are indicated at channels 438 and 460, respectively. The Ag impurity distribution also does not appear to change with varying PLM fluence. Thus, increasing the PLM fluence only improves the quality of epitaxy slightly, without affecting the post-PLM Ag distribution (along the direction of epitaxy). Note that these observations are not a result of insufficient melt depths during PLM,[41] but instead are due to increasing melt depths and hence solidification times, as will be discussed later.

Furthermore, the channelled and random Ag signals for every PLM fluence shown in Fig. 1(b) were also identical to each other (all the random spectra have not been plotted for clarity). Thus, there is no observable preferential lattice site for Ag, but rather it appears to be randomly located within the defective region of the Si lattice. Indeed, RBS-C angular scan profiles for Ag, obtained over the top 80 nm layer of the (defective epitaxy) sample and including the surface segregated Ag layer, confirm this conclusion. This angular scan is shown in Fig. 2. A dip/minimum is expected for substitutional atoms (due to shadowing of subsurface atoms within atomic rows) when the incident RBS He^+ beam is aligned with the <100> axial channel of the sample. This is typically achieved with a sample tilt angle of $\alpha \sim 0°$. Conversely, interstitial atoms located at the center of the channel will result in a peak/maximum at $\alpha \sim 0°$ that is greater than the random yield due to a flux peaking effect of the incident RBS He^+ beam when it is well aligned.[37] Thus, the featureless nature of the Ag profile in Fig. 2, in comparison with the strong expected dip in the Si yield, strongly suggests that no measurable fraction of Ag atoms is preferentially located on substitutional or interstitial positions within the Si lattice.[37] This behavior is unlike Au-hyperdoped Si, where the Au impurity has a significant substitutional lattice location,[9,20,25] indicated by its U-shaped profile in Fig. 2 taken from Ref. 25.

We now investigate the SIMS measured Ag distribution profiles of the same samples, shown in Fig. 3. SIMS was employed due to its much lower detection noise floor than RBS. A linear concentration scale was used in Fig. 3(a) to aid comparison with RBS measurements in Fig. 1(b), while the log scale in Fig. 3(b) better illustrates that the Ag concentration tail extends even deeper into the substrate. We note again that the shoulder feature in the Ag as-implanted profiles at around 90 nm is due to Ag diffusion in the amorphous layer during low temperature annealing, as discussed earlier. After PLM, Ag segregation toward the surface was observed in the $3 \times 10^{15}\,\mathrm{cm}^{-2}$ (good epitaxy) sample [more obvious in Fig. 3(a)], in agreement with RBS. It is important to note that the SIMS yield is not accurate in the first 15 nm below the surface due

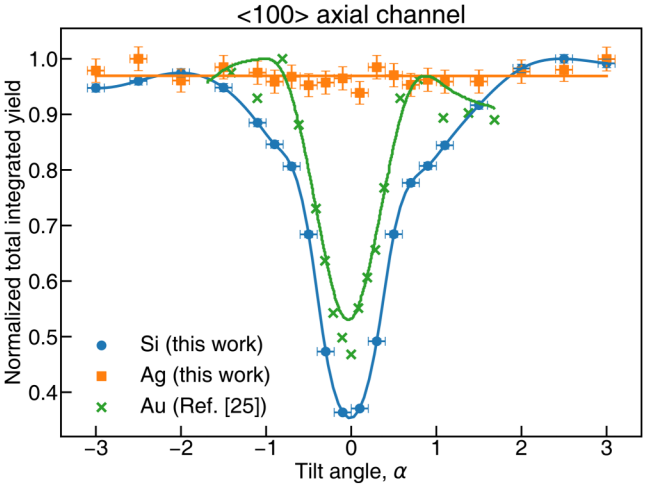

FIG. 2. RBS-C angular scan profiles for Si–Ag (measured on the 80 keV Ag $1 \times 10^{16}\,\mathrm{cm}^{-2}$ sample irradiated at $0.91\,\mathrm{J/cm}^2$) and Si–Au (Ref. 25). The Si–Ti angular scan profile (measured on the 45 keV Ti $3 \times 10^{15}\,\mathrm{cm}^{-2}$ sample irradiated at $0.90\,\mathrm{J/cm}^2$) was similar to Si–Ag shown and thus not plotted for clarity. Profiles were normalized to their corresponding maxima (approximately the random level) to aid comparison. Solid lines are plotted to guide the eye.

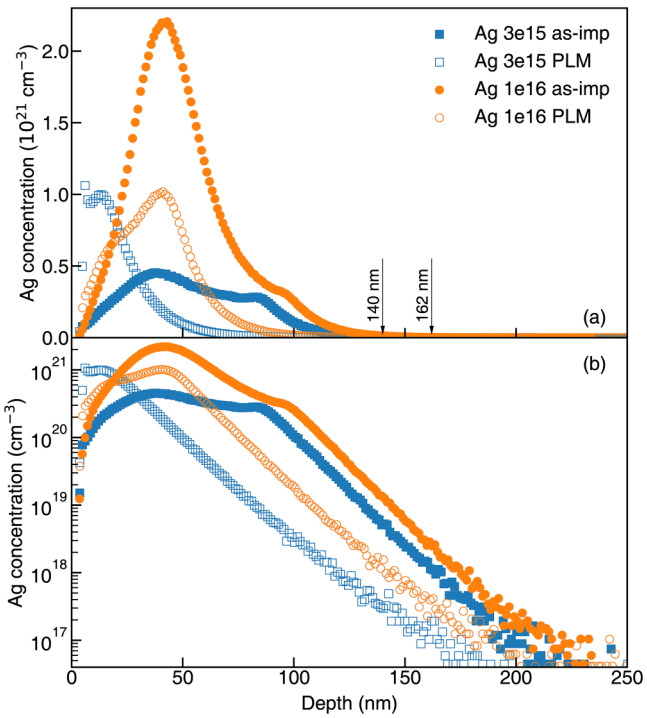

FIG. 3. SIMS profiles for the Ag impurity in the as-implanted (solid) and PLM (1.10 J/cm^2) (hollow) Ag 3×10^{15} cm^{-2} (good epitaxy) (blue) and 1×10^{16} cm^{-2} (defective epitaxy) (orange) samples plotted on a (a) linear and (b) log scale. Arrows indicate the amorphized depths of each sample following implantation and a low temperature pre-anneal.

to measurement artifacts partly related to a native oxide and transient effects,[42] and thus the surface Ag peak can be absent in SIMS (Fig. 3) despite its marked presence in RBS (Fig. 1). We further note that a surface segregation peak is also expected from diffusion calculations.[41] Thus, in the 3×10^{15} cm^{-2} (good epitaxy) sample, the maximum Ag concentration attained after PLM (1×10^{21} cm^{-3}) must be located at the surface, which then decreases exponentially toward the substrate. Furthermore, it is clear that, although there is a long Ag concentration tail that extends deep into the substrate [Fig. 3(b)], it is at a concentration several orders of magnitude lower than the surface Ag, ascribed to depth resolution exponential tailing[42] (i.e., it is a SIMS artifact). On the other hand, in the Ag 1×10^{16} cm^{-2} (defective) sample, a significant amount of Ag was trapped beneath the surface after PLM, with up to 1×10^{21} cm^{-3} Ag 40 nm away from the surface. These SIMS data are all in very good agreement with RBS.

Thus far, it appears that a significant amount of Ag trapping is only obtained when defective epitaxy occurs during PLM. Conversely, good epitaxy results in almost complete Ag surface segregation. Further insight into the defective nature of the 80 keV Ag 1×10^{16} cm^{-2} sample can be gained from TEM and APT measurements, shown in Figs. 4 and 5(a), respectively. From Fig. 4(a), it is clear that the top 70 nm layer of the material is visibly defective, in good agreement with the disorder observed by RBS-C. Unsurprisingly, Fig. 4(a) strongly resembles a typical TEM micrograph of materials that have endured filamentary breakdown, a phenomenon commonly observed in transition metal-hyperdoped Si fabricated from implantation and PLM.[20,22,29,31,43] The darker strands extending from the surface are known as "filaments" and contain a disproportionately high concentration of Ag in comparison to the lighter Si regions in between, confirmed by energy dispersive x-ray spectroscopy (EDS) (not shown).

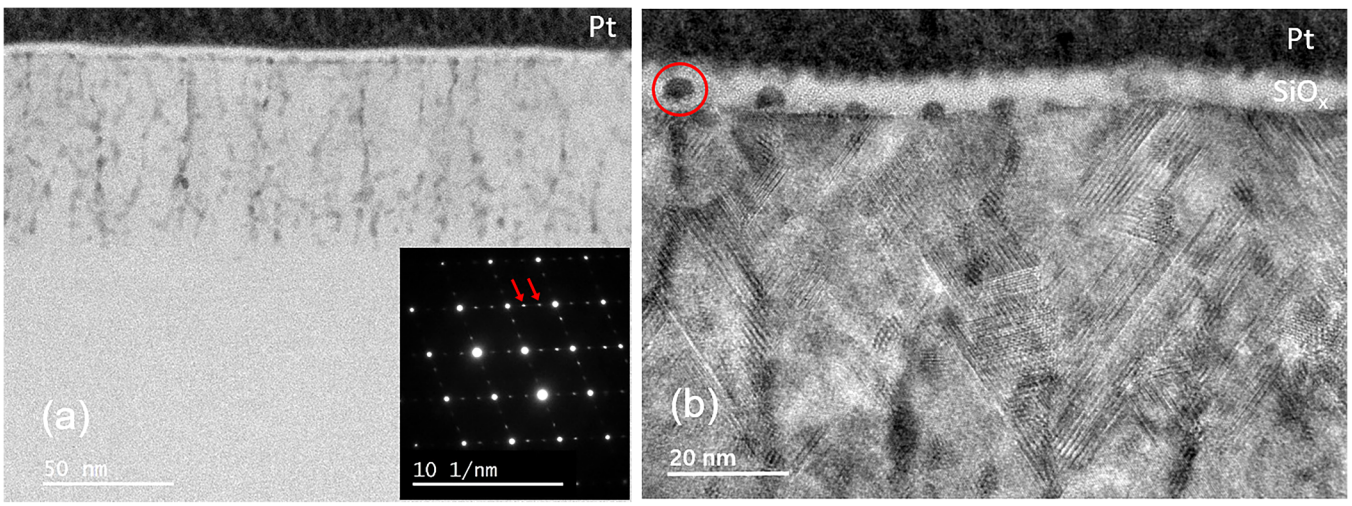

FIG. 4. (a) and (b) TEM micrographs for the 80 keV Ag 1×10^{16} cm^{-2} (defective epitaxy) sample that received a PLM fluence of 0.95 J/cm^2, taken under different imaging conditions. In (a), a highly defective surface layer comprising filament-looking structures was observed. (b) is a magnification of (a), showing the widespread presence of stacking-like defects within the filamentary layer. (Inset) SAED pattern obtain from a region containing both the defective surface layer and underlying Si substrate. Fainter but visible diffraction spots (indicated by red arrows) between the brighter Si reflections are evidence for the 9R-Si phase.

Furthermore, there is no evidence of Ag precipitation. The filamentary nature of our samples is further supported by APT measurements that we show later.

Upon closer inspection of the filamentary layer [Fig. 4(b)], stacking-like defects become apparent and are unevenly distributed across the filament-decorated layer. The inset of Fig. 4(a) is a selected area electron diffraction (SAED) pattern measured from a region containing these defects and filaments. Surprisingly, this diffraction pattern (two equally spaced, weaker reflections at 1/3 and 2/3 distances between the brighter diamond cubic Si reflections) closely resembles that of hexagonal 9R-Si structures previously observed for Kr^+ implantation into SiO_2/Si.[44] To our surprise, the formation of hexagonal 9R-Si regions in filamentary material is not unusual. Similar TEM and SAED observations have been reported in hyperdoping experiments involving Si implanted with very high doses of Au ($> 6 \times 10^{15}$ cm^{-2}),[20,25] although in this case the authors did not associate these stacking-like defects with the 9R-Si phase. We believe that the formation of 9R-Si in filamentary materials is stimulated by stress[44] due to the presence of high and laterally non-uniform impurity concentrations. Ag-rich nanoparticles (containing Ag, Si, and O) measuring about 5 nm in diameter were also observed within the surface oxide layer. An example of such a nanoparticle is highlighted by a red circle in Fig. 4(b). There is no evidence of Ag precipitation or the formation of secondary Si–Ag phases within these nanoparticles nor within the filaments. This is expected since such equilibrium phases typically form over time scales that are much longer than the solidification time of our samples following PLM (tens of nanoseconds). Rather, high resolution TEM images of the filaments (not shown) suggest that they most likely comprise of a crystalline mixture of Si and Ag. Note that TEM performed on the 80 keV Ag 3×10^{15} cm^{-2} sample (good epitaxy) showed pristine quality crystalization post-PLM (not shown), in excellent agreement with RBS, with no signs of Ag nanoparticles or precipitation at least to within the resolution of TEM and EDS (1 at. % Ag). These TEM data are also in good agreement with atom force microscopy measurements presented in Appendix B in the supplementary material, all showing no evidence of Ag nanoparticle formation on the surface of the 80 keV Ag 3×10^{15} cm^{-2} sample.

We now examine the APT measurements. A representative 3D APT reconstruction of a filament is shown in Fig. 5(a). The gray surface on the left is a 1 at. % Ag isoconcentration surface. On the right is the same filament neighborhood represented by isoconcentration contour intervals of 1 at. %. The high concentration region on the far right of the filament is a digital edge artifact. From Fig. 5(a), it appears that the filamentary layer consists of not only branched filaments, but also Ag-rich droplets between and at the end of filaments. Both filaments and droplets measured about 5 nm in width and extend to about 60 nm from the surface, reasonably consistent with TEM and RBS-C. The central Ag composition of the filament slice in Fig. 5(a) is about 8–10 at. %, while the average central Ag composition from droplets and branched filaments throughout the material is around 24 at. %. Thus, the filaments are mixtures of Ag and Si of varying compositions, consistent with previous reports on Si–Co.[43] There are also definite signs of breakdown structures within the thickened surface oxide (6–8 nm). Furthermore, oxygen mapping (not shown) suggests that there is oxygen segregation to the outside surface of the filaments just beneath the surface oxide region. Interestingly, there were also significant amounts of Ag segregated just below the surface oxide of the sample in the bulk Si regions between filaments, but not actually within the surface oxide itself. In other words, Ag in the surface oxide layer is only present in breakdown structures.

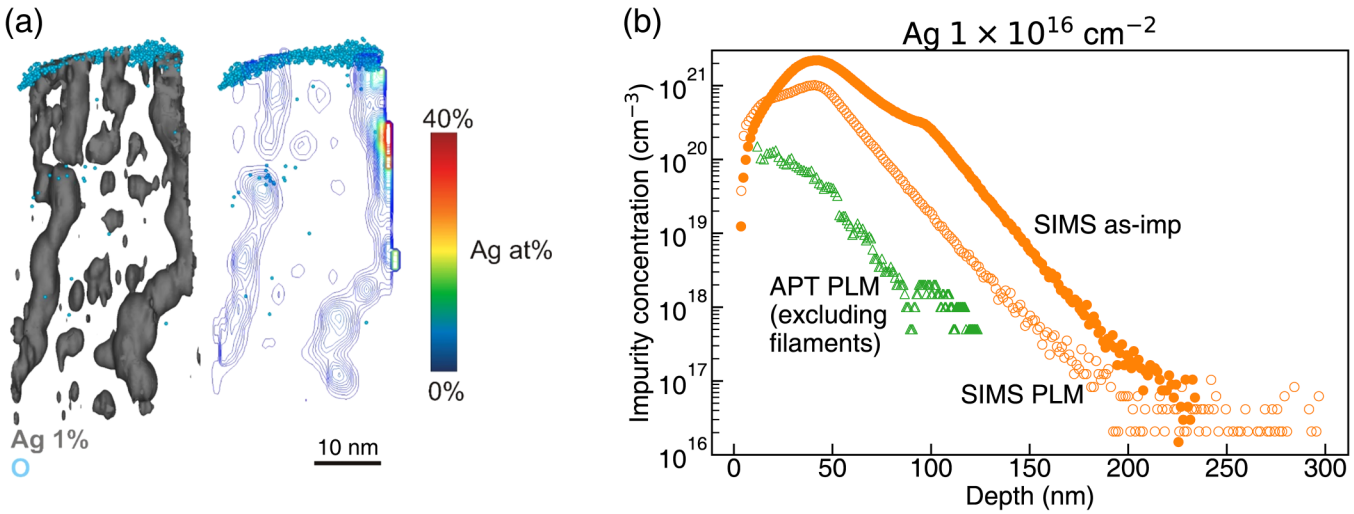

FIG. 5. (a) (Left) APT reconstructed 3D image of a small neighborhood containing Ag-rich branched filaments and droplets. The gray surface is a 1 at. % isoconcentration surface. (Right) Isoconcentration contour plot of the same filament, plotted with 1 at. % contour intervals. (b) APT measured Ag concentration profile in regions *excluding* the filaments and droplets (green triangles), plotted alongside SIMS data from Fig. 3(a) (orange circles).

Figure 5(b) shows the APT measured Ag concentration-depth distribution of the same sample performed in regions *excluding* the filaments and droplets [i.e., white region in Fig. 5(a)], represented by green triangles. On the other hand, the orange circles are SIMS measurements performed on the same sample and have previously been shown in Fig. 3(a). Note that the near atomic resolution of APT enabled us to perform measurements in more refined regions that exclude the filaments, unlike SIMS and RBS (including angular scans) which measure the compositional average over a much larger area (hundreds of micrometers in diameter) containing both the filaments and surrounding regions. Once again, APT revealed that the highest Ag concentration is located at the surface and decreases exponentially with depth. More specifically, the maximum Ag concentration in regions excluding the filaments is ~0.2 at. % (or 10^{20} cm^{-3}), attained only at the surface. This is more than 10 times less than the SIMS maximum of ~4 at. %. Furthermore, the Ag concentration in regions excluding the filaments is at least 100 times less than the average *central* composition of filaments (i.e., average of the maximum filament compositions). Thus, practically all of the trapped Ag in our defective epitaxy samples is present within filament structures.

B. Si–Ti system

As there has already been prior TEM and APT measurements on similar Si–Ti samples published in the literature, we will only show our RBS-C and SIMS results here, while supporting TEM data can be found in Appendix C in the supplementary material. However, we do provide a review of the results of TEM and APT measurements in the literature in Sec. IV and discuss their relevance to our results. Similar to Si–Ag, RBS-C suggests that, depending on the Ti implantation dose, PLM will result in either good epitaxy and complete Ti surface segregation or defective epitaxy associated with filamentary breakdown. Figures 6(a) and 6(b) are RBS spectra for the 45 keV Ti 1.5 × 10^{15} cm^{-2} and 3 × 10^{15} cm^{-2} samples, respectively. From the channelled Si signal post-PLM in Fig. 6(a), at first glance it appears that the sample has solidified with good epitaxy after PLM (fluence ≥0.75 J/cm^2). The identical channelled and random Ti signals suggest that there is no significant fraction of substitutional or interstitial Ti above the RBS detection limit (~10^{19} cm^{-3}). However, it is important to note that the TEM of this sample (shown in Appendix C in the supplementary material) revealed the presence of some early-stage Ti-rich filaments within the top 20 nm beneath the surface oxide, with no evidence of stacking-like defects. In particular, the filament density in this sample is much lower than that of the Ti 3 × 10^{15} cm^{-2} and Ag 1 × 10^{16} cm^{-2} samples in this work and similar to Si–Ti samples reported in the literature.[29,45] Nevertheless, the bulk of the material displayed excellent crystal quality. Note that our TEM results do not contradict with RBS-C measurements shown in Fig. 6(a). Rather, our results imply that RBS-C is not always sensitive enough to pickup filamentary breakdown behavior, especially when it is at its early stages. Furthermore, the presence of these early-stage filaments, and hence the start of lateral segregation of Ti at the melt–solid interface as it approaches the surface, will lead to Ti-rich regions which will give rise to an emerging "tail" in RBS spectra,[37] as observed.

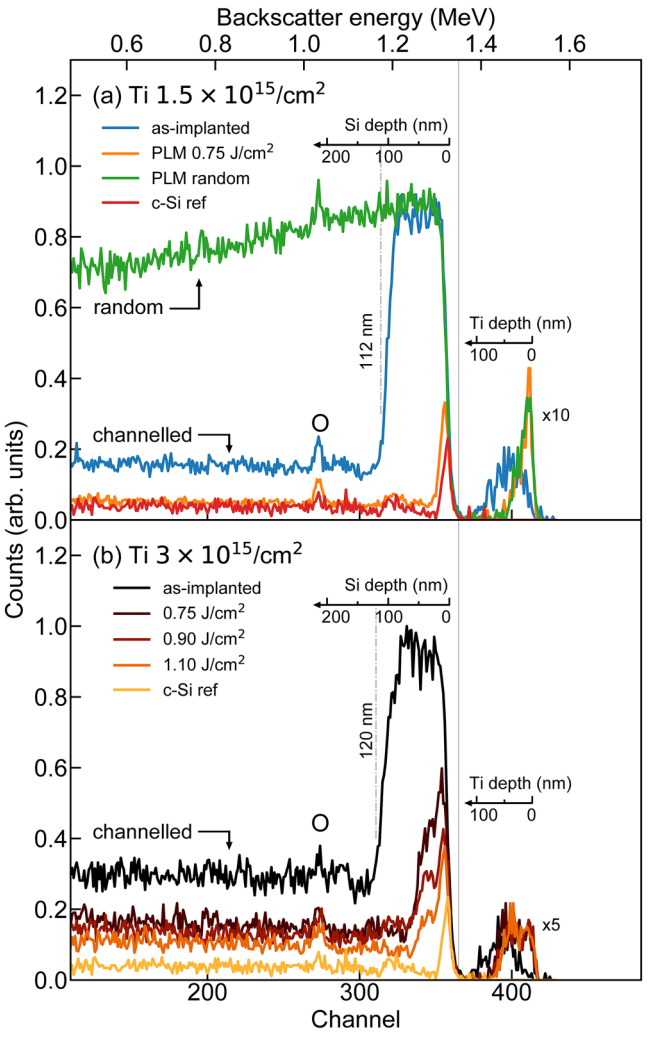

FIG. 6. RBS spectra for 45 keV Ti (a) 1.5 × 10^{15} cm^{-2} (PLM 0.75 J/cm^2) and (b) 3 × 10^{15} cm^{-2} samples subjected to PLM at different laser fluences. The Ti RBS signal was amplified for clarity. The as-implanted spectrum and a pristine Si reference spectrum (c-Si ref) are also shown to aid comparison.

On the other hand, in Fig. 6(b), for the Ti 3 × 10^{15} cm^{-2} sample, the Si signal appears very similar to that of Ag 1 × 10^{16} cm^{-2} in Fig. 1(b), where the broad features between channels 330 and 360 are indicative of defective epitaxy following PLM. The spectrum for the sample receiving a PLM fluence of 1.40 J/cm^2 was identical to that of a 1.10 J/cm^2 fluence sample and thus not plotted for clarity. Indeed, having understood the filamentary nature of the defective layer in Si–Ag, one can interpret these defect features to be a manifestation of filamentary breakdown, as will be discussed later. As for the Ti signal, significant quantities of Ti were trapped within the defective layer in addition to some Ti surface segregation. The Ti distribution also does not change with PLM fluence. Similar observations were found in the 5 × 10^{15} cm^{-2} sample.

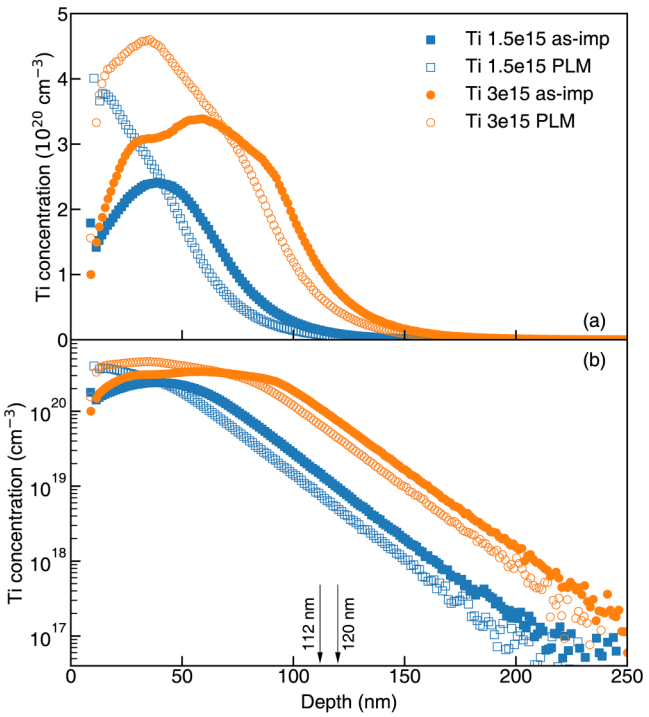

FIG. 7. SIMS profiles for the Ti impurity in the as-implanted (solid) and PLM (1.10 J/cm^2) (hollow) Ti 1.5×10^{15} cm^{-2} (good epitaxy) (blue) and 3×10^{15} cm^{-2} (defective epitaxy) (orange) samples plotted on a (a) linear and (b) log scale. Arrows indicate the amorphized depths of each sample following implantation and a low temperature pre-anneal.

RBS-C angular scan profiles were also measured for the Ti 3×10^{15} cm^{-2} defective sample (along <100> and obtained for the top 60 nm surface layer) and were flat and essentially identical to that of Ag (not plotted for clarity, see Fig. 2), in good agreement with previous measurements performed by Liu *et al.*[30] Thus, the Ti atoms are neither preferentially substitutional nor interstitial in Si after PLM, at least within the resolution of RBS-C. Instead, they are *randomly oriented* throughout the Si layer.[37]

The measured SIMS Ti concentration-depth profiles of both the Ti 1.5×10^{15} cm^{-2} and 3×10^{15} cm^{-2} samples are shown in Fig. 7. Once again, we plot the Ti concentration on linear and log scales to aid discussion. Some Ti diffusion occurred in the as-implanted samples for similar reasons discussed previously for Ag. A long Ti impurity tail that extends deeper into the substrate, due to the aforementioned SIMS artifact (depth resolution exponential tailing),[42] was observed in all the samples, although at concentrations much lower than at the surface. In the 1.5×10^{15} cm^{-2} sample, after PLM, a significant portion of Ti has segregated to the surface, although there does appear to be Ti trapped within the top 100 nm surface layer. In this case, the indication of Ti retained below the surface could again relate to the early-stage filaments and lateral Ti segregation mentioned above. On the other hand, in the 3×10^{15} cm^{-2} sample, much less Ti surface segregation was observed, with significant amounts of Ti remaining trapped within the top 100 nm of the material, presumably within filaments. Thus, our SIMS observations are consistent with RBS, noting again that the Ti surface segregation peaks do not appear in SIMS due to the aforementioned SIMS surface artifact.

IV. DISCUSSION

Before proceeding with our discussion, we first provide an overview of previous TEM and APT measurements performed on similarly implanted and PLM-processed Si–Ti samples.[8,29,31,45] Briefly, either complete Ti surface segregation or filamentary breakdown was observed in <100> Si samples implanted with 32 keV Ti $10^{13} - 10^{15}$ cm^{-2} and 10^{16} cm^{-2}, respectively, following PLM.[45] TEM confirmed that the latter Si–Ti sample exhibited filamentary breakdown behavior, while SAED measurements revealed the same 9R-Si phase that was also observed in Si–Ag [Fig. 4(c)].[45] The maximum Ti concentration that was homogeneously incorporated in the Ti 10^{15} cm^{-2} sample is 10^{21} cm^{-3} at 10 nm from the surface (measured from SIMS), with less than 20 nm containing Ti above N_{IB}. Filamentary breakdown was also reported in <111> Si implanted with high doses of Ti (10^{16} cm^{-2}). At lower Ti doses, significant Ti surface segregation was accompanied by solidified material that contained defects suggested to be stacking faults[46,58,59] rather than defect-free recrystallization.[8,29] Subsequent APT concentration profiling measurements performed in regions excluding the filaments indicated that, just like Ag, all of the measurable Ti is confined within the filaments.[31] There is also no evidence of Ti precipitates and/or nanoparticles.

We now summarize our results and discuss their significance in relation to the hyperdoping literature. Thus far, we have shown that both Si–Ag and Si–Ti behave very similarly in our experiments, namely, above a certain threshold implant dose, D_b, defective epitaxy associated with filamentary breakdown occurs following PLM, while below D_b good quality epitaxy (in <100> Si) accompanied by near complete impurity surface segregation occurs. This is in very good agreement with similar experiments in the literature involving Co, Cu, Fe, Zn, Mn, W, Mg, Cr, and Yb in Si.[22,41] Note that from here on, samples that recovered with good quality and defective epitaxy following PLM will be interchangeably referred to as samples implanted below and above D_b, respectively, noting that D_b generally varies with the specific PLM conditions such as the laser wavelength and pulse duration.[47]

A comparison between <100> Si–Ag (80 keV), Si–Ti (45 keV), and Si–Au (300 keV)[20,25] implanted samples subjected to PLM is provided in Table II. Interestingly, Au is the exception among the transition metals under similar hyperdoping experiments since it can be trapped in substitutional lattice sites in Si at concentrations much higher than any other transition metal impurity to date.[9,12,20,22,48] Nevertheless, increasing the Au implant dose inevitably leads to filamentary breakdown,[20,22] just like Ag, Ti, Co,[43] and many other metals.[22,41] This is because increasing the implant dose (i.e., the impurity concentration) results in greater local melting point depressions in regions containing higher concentrations of rejected metal impurities. This effect amplifies the solid–liquid interface roughness and associated instabilities during rapid solidification. Consequently, in addition to surface

segregation, substantial impurity segregation in the lateral direction occurs, forming spatially confined and impurity-rich filaments, much like conventional cellular breakdown.[29,41,43,49] Longer solidification times associated with higher PLM fluences would thus result in further segregation of impurities both toward the surface and laterally toward the center of filaments. In particular, it is possible that further lateral impurity segregation due to longer solidification times may result in a slight increase in volume of material with improved crystallinity. Indeed, this is what we observed in our Si–Ag and Si–Ti RBS spectra shown in Figs. 1(b) and 6(b), where the subsurface defect amplitude decreases with increasing PLM fluence. Moreover, since lateral impurity segregation prevails, the Ag or Ti distribution in the direction of epitaxy and the average length of filaments (i.e., the thickness of the defective layer) do not change with increasing PLM fluence (discussion about random fluctuations in the PLM fluence can be found in Appendix A of the supplementary material).

Highly substitutional trapping of Au was not only observed in Si–Au samples implanted below D_b, but also in those implanted above D_b that resulted in filamentary breakdown.[20,25] Furthermore, it has been shown that the substitutional Au concentration after PLM in both samples implanted below and above D_b can significantly exceed N_{IB}, the concentration needed to form a Au-induced impurity band.[9,20] In particular, for Si–Au samples implanted above D_b, high concentrations of substitutional Au were detected both outside and within the filaments.[20] Thus, it is extremely likely that a Au impurity band has formed in the Si bandgap of both these types of Si–Au materials.

However, unlike Au, based on the high degree of surface segregation and the lack of preferred impurity lattice site location, we do not expect impurity bands to form in our Si–Ag or Si–Ti samples. In particular, for samples implanted above D_b, APT performed in regions excluding filaments [Fig. 5(a)] indicated that $N_{Ag} > N_{IB}$ only within the top 20 ± 5 nm surface layer, while for Ti such a surface layer with $N_{Ti} > N_{IB}$ is only about 5 nm thick.[31] Furthermore, it is evident from channelling and angular scan measurements that Ag and Ti do not have a preferential lattice location in samples implanted above D_b, at least within the resolution of RBS (which is below N_{IB}). Hence, it is also extremely unlikely that there is any significant common lattice location in samples implanted below D_b. Consequently, despite having thin surface layers of materials where the condition $N_{Ag}, N_{Ti} > N_{IB}$ is marginally satisfied, we believe that there will be insufficient concentrations of opto-electrically active Ag or Ti to form an impurity band anywhere in the material[52,60] (see Table II for the required impurity configuration). Thus, for the purposes of optical hyperdoping to achieve an impurity band in Si, neither Ag nor Ti is suitable.

It is also worth mentioning that the estimated range of D_b that we report here for <100> Si–Ti (45 keV) is lower than that of <111> Si–Ti (15 keV) in Ref. 29, where D_b of the latter was determined to be $(3\text{-}10)\times10^{15}$ cm^{-2}. This is primarily due to the different implantation energies involved, in addition to the substrate orientation.[53] Since a lower implantation energy results in a shallower implant range and amorphous layer, lower PLM fluences (and thus shorter solidification times) are required to melt beyond the amorphous–crystal interface for high quality liquid-phase epitaxy. Therefore, there is simply less time for interfacial instabilities to amplify and develop into filamentary structures, and consequently D_b is higher in Si–Ti (15 keV). We further note that the difference in D_b between Si–Ag and Si–Ti (despite having a similar implant end of range of ~100 nm) is most likely due to specific differences in their metal-silicon eutectic properties and values for k',

TABLE II. Summary of key observations from implantation and PLM experiments in this work (Ag, Ti) and similar RBS and TEM experiments in Refs. 20 and 25 (Au). This comparison clearly shows that Au is superior to both Ag and Ti for hyperdoping in Si in terms of trapping in the solid in opto-electrically active sites both below and above D_b. We note that although 300 keV Au has a deeper impurity profile and as-implanted amorphous thickness (~300 nm) than our Si–Ag (~150 nm) and Si–Ti (~115 nm) samples, it was previously shown that Si–Au samples prepared at lower implantation energies display similar behavior as these 300 keV Si–Au samples in terms of substitutional trapping and breakdown.[9,25,48] Thus, the different implantation energies only affect D_b. Note that all of these results (for Au, Ag, and Ti) were observed in <100> Si substrates under similar PLM conditions (355 nm YAG laser, 6 ns pulse duration).

	Si–Ag (80 keV)	Si–Ti (45 keV)	Si–Au (Refs. 20 and 25) (300 keV)
Threshold dose (D_b) (cm^{-2})	$(3\text{-}10)\times10^{15}$	Slightly below 1.5×10^{15}	$(2\text{-}6)\times10^{15}$
Below D_b: observation	Good epitaxy and complete Ag surface segregation	Good epitaxy and complete Ti surface segregation	Good epitaxy, both Au substitutional trapping and partial surface segregation observed
Below D_b: surface impurity concentration	$>6\times10^{19}$ cm^{-3} at the top 5 nm layer	$>6\times10^{19}$ cm^{-3} in the top 40 nm layer	N/A
Impurity lattice location	Neither substitutional nor interstitial	Neither substitutional (s) nor interstitial (i)	Preferentially substitutional
Electrically active impurity (D: donor; A: acceptor) (eV)[4,50,51]	Ag_s, Ag_{s-i} (D)$E_V+0.38$ (A)$E_C-0.55$	Ti_i (D)$E_C-0.27$ (DD)$E_V+0.28$ (A)$E_C-0.08$	Au_s (D)$E_V+0.34$ (A)$E_C-0.55$
Above D_b: observation	Filamentary breakdown with no specific atom location	Filamentary breakdown with no specific atom location	Filamentary breakdown and substitutional Au both inside and outside filaments

the non-equilibrium interfacial distribution coefficient (or sometimes known as the partition coefficient).[22,41] However, the thick surface oxide (6–8 nm) in the Si–Ag samples after PLM was not observed in Si–Ti,[29,31] although it has been observed in Si–Au.[20] One possible explanation is that, like Au, Ag is acting as an oxidation catalyst to Si.[54,55] The presence of spherical, Ag-rich nanoparticles within the surface oxide [Fig. 4(b)] has also never been reported in the literature.[20,22,43] We do not currently have an explanation for this, due to limited knowledge about Ag precipitation in Si in the literature.[4]

It is important to note that filamentary breakdown has subtle structural differences compared with conventional cellular breakdown. The latter is characterized by columns of cell-wall-like structures extending from a surface cellular network and has appeared in experiments involving Si heavily implanted with As, In, Ga, Bi, and Sb followed by PLM.[49] Indeed, earlier implantation and PLM experiments reporting cellular breakdown phenomena in Si frequently involved the more traditional group III and V dopants.[41] This is in contrast to filamentary breakdown, which does not necessarily exhibit the characteristic cellular structures on the surface and appears to be more common in similar experiments involving transition metal impurities (Ag, Ti,[31] Au,[20] Co[43]). It also appears to be difficult, if not impossible, to differentiate between cellular and filamentary breakdown without APT, as they can both appear similar in TEM[41,49] (note that there is a lack of APT data on conventional cellular breakdown in the literature). Thus, it is reasonable to infer that several previous reports of cellular breakdown in Si implanted with high doses of Cu, Fe, Zn, Mn, W, Mg, Cr, or Yb followed by PLM (characterized by TEM), are, in fact, filamentary (and not cellular) breakdown. However, it is also possible that the two breakdown regimes are distinguished only by the solidification time scales during PLM. In other words, "filaments" are likely to be a transient product of amplified morphological instabilities at the solid–liquid interface and should eventually evolve into "two-dimensional blades" and finally "call-walls," given sufficient time.[31] Nevertheless, both regimes, filamentary and cellular, limit the concentration of impurity that can be uniformly trapped in good quality crystalline Si. We further refer readers to Refs. 31 and 43 for a more in-depth treatment on the topic.

To summarize, our experiments have clearly demonstrated that both Ag and Ti are not suitable for hyperdoping in Si, as there is simply insufficient opto-electrically active Ag_s and Ti_i for an impurity band to form. This is regardless of whether the material exhibits filamentary breakdown or near-complete impurity segregation. Although we do not rule out the possibility of having large opto-electrically active multi-atom complexes within filaments, the impurity-rich Si material is nevertheless highly defective, and it would be impossible to isolate optical and electrical responses from such multi-atom complexes from those from crystalline defects. We note that our conclusions for Si–Ti are consistent with those put-forth by Mathews *et al.*[29] and Liu *et al.*[30] Even though improved sub-bandgap absorption and conductivity were clearly demonstrated for such Si–Ti materials,[6,16,18,30] interestingly, the NIR responsivity of photodetectors fabricated from these Si–Ti materials was surprisingly low ($\sim 10^{-2}$ V/W).[8,45] This fact does not appear to be consistent with the corresponding optical and electrical measurements. Since these anomalies cannot be attributed to a Ti impurity band[7] or the dilute concentrations of soluble Ti_i,[30] it is far more likely that they originate from the high density of defects within the material and/or the complex interactions of these defects with the metal impurity atoms/filaments.[1,20,26,30,44,56] Thus, it is reasonable to expect photodetectors fabricated from these defective and filament-rich materials (whether Si–Ag or Si–Ti) to exhibit high reverse leakage currents and poor photo-carrier transport properties as suggested also by García-Hemme *et al.*,[8] subsequently degrading detection sensitivity and efficiency. We, therefore, do not believe that these defective materials are suitable for high efficiency Si-based photodetection. It is also worth mentioning that "Ag-hyperdoped Si" was claimed to be fabricated from thin film Ag deposition and femtosecond-PLM (not nanosecond), *followed by a 30 min 800–1000 °C anneal*.[24] However, based on our findings it is highly unlikely that opto-electrically active Ag-hyperdoping was achieved in this case. In particular, it is very surprising that the Ag concentration profiles before and after a 950 ° furnace anneal were identical, given the high diffusivity of Ag in solid Si even at moderate temperatures below 900 °C.[4] Furthermore, as mentioned previously, femtosecond lasers can result in spiky surface microstructures that are highly defective and absorbing in the infrared.[27,28] Further investigations related to the effect of using femtosecond-PLM on the material crystallinity and its surface, as well as the Ag atom location, would thus be necessary to better understand the photo-electrical anomalies reported in Ref. 24.

Finally, it is pertinent to realize that, despite numerous efforts at trying to fabricate metal-hyperdoped Si materials, Au is the only metal impurity to date that has achieved sufficiently high subsurface concentrations in near-defect-free single-crystal Si material necessary for impurity band formation. Unfortunately, it has been difficult to establish the factors that lead to this success for Au in comparison with other transition metals in such hyperdoping experiments. This is largely due to the decidedly empirical nature of key parameters involved during the ultra-rapid solidification process following PLM, such as the partition coefficient k' (related to the ratio between the solubility of an impurity in liquid and solid), metal diffusivities in the liquid and at the solid–liquid interface, and intrinsic defects that can affect the diffusion mechanism of the impurity in the solid near the interface. Parameters such as k' also depend on the melt front velocity and will need to be determined for each unique set of PLM conditions (7–10 m/s in our experiments[22]). The diffusive velocities of metals such as Ag and Ti in liquid Si are also not known accurately.[22] Thus, at present, suitable metal impurities for hyperdoping in Si cannot be reliably predicted, but must be ascertained through experimental investigation, such as in the current study. At first sight, this is not particularly good news for advancing research in the Si hyperdoping field. However, we can offer some potentially fruitful approaches that do not involve extensive experimental investigations and analyses. Indeed, we have shown that impurities at low implant doses that strongly segregate to the surface during PLM (such as Ag and Ti) are not likely to be trapped at hyperdoping concentrations under any laser conditions. Hence, in surveying other suitable deep level impurities as hyperdoping candidates, first undertaking PLM on low dose implanted Si, followed by SIMS or RBS to determine the degree of segregation, can guide the selection of potentially suitable impurities for further more detailed study. In addition, we propose

that the higher Z transition metals (specifically, the third row of the transition metals in the periodic table) are more likely to achieve successful hyperdoping than the lower Z species due to the following reasons: (1) most of the low Z transition metals in the first row have already been shown to be strongly segregating at doses before breakdown;[22,41] (2) Cu, Ag, and Au have similar valence shell electronic configurations (they occupy the same column on the periodic table) but Cu and Ag are strongly segregating species while Au is not; (3) there is evidence in the literature that Pt can be incorporated into substitutional Si lattice sites through implantation and subsequent nanosecond-PLM just like Au.[57] Thus, we propose that Pt and W (and other metals in the same row) could be potential species to be examined in future optical hyperdoping experiments.

V. CONCLUSION

To conclude, we have shown that neither Ag nor Ti are suitable for hyperdoping in Si as the maximum opto-electrically active impurity concentration that can be incorporated in monocrystalline Si is below the concentration needed for impurity band formation. In particular, when good quality epitaxy was observed (below D_b), it was accompanied by near-complete impurity surface segregation following PLM. On the other hand, in samples implanted above D_b, defective epitaxy associated with filamentary breakdown was observed. The near-atomic resolution of APT enabled us to perform detailed impurity distribution mapping of the breakdown layer, indicating that practically all of the Ag (and Ti) atoms are confined to within filamentary structures. Furthermore, channelling measurements suggest that both Ag and Ti are randomly oriented in the Si lattice after PLM, and thus the opto-electrically active Ag and Ti concentrations are substantially lower than the maximum measured by SIMS and APT in the near-surface. Even if it is possible for large opto-electrically active multi-atom complexes to exist within filamentary structures, the highly defective nature of this material makes it unsuitable for high efficiency light detection. Our experiments also demonstrated that techniques such as RBS-C (and its related angular scans) and APT are necessary in addition to SIMS and TEM to obtain a comprehensive picture of the physical nature of the material, especially since SIMS, which is more sensitive than RBS, is known to be unreliable close to the surface and introduces "erroneous tails." The impurity lattice location and distribution (both normal to the surface and laterally), in addition to the quality of epitaxy after PLM, are all crucial factors for determining the suitability of metal-Si systems as an impurity band semiconductor for Si-based NIR opto-electric applications.

SUPPLEMENTARY MATERIAL

See the supplementary material for melt duration data and discussions related to random errors in the nominal PLM fluence (Appendix A); atom force microscopy measurements of the Ag samples (Appendix B); and a TEM micrograph of the 45 keV Ti 1.5×10^{15} cm^{-2} sample (Appendix C).

ACKNOWLEDGMENTS

The authors acknowledge the U.S. Army (Contract No. FA5209-16-P-0104) for financial support of this project. S.Q.L. and J.S.W. thank Professor J. Bradby for useful discussions related to the 9R-Si phase, Dr. L. Huston for TEM assistance, and Dr. C. Notthoff for assistance with atom force microscopy. The authors acknowledge AFAiiR and ANFF ACT-node for access and technical support to ion beam and fabrication facilities.

DATA AVAILABILITY

The data that support the findings of this study are available from the corresponding author upon reasonable request.

REFERENCES

[1]H. Y. Fan and A. K. Ramdas, J. Appl. Phys. **30**, 1127 (1959).
[2]A. P. Knights, A. A. House, R. MacNaughton, and F. Hopper, in *Optical Fiber Communication Conference* (Optical Society of America, 2003), p. FJ3.
[3]M. W. Geis, S. J. Spector, M. E. Grein, R. T. Schulein, J. U. Yoon, D. M. Lennon, S. Deneault, F. Gan, F. X. Kaertner, and T. M. Lyszczarz, IEEE Photon. Technol. Lett. **19**, 152 (2007).
[4]K. Graff, *Metal Impurities in Silicon-Device Fabrication* (Springer Science & Business Media, 2013), Vol. 24.
[5]Note that the chalcogens (S, Se, Te) have also been studied extensively for hyperdoping in Si, but we focus only on the metals in this work.
[6]J. Olea, G. González-Díaz, D. Pastor, and I. Mártil, J. Phys. D **42**, 085110 (2009).
[7]J. Olea, M. Toledano-Luque, D. Pastor, E. San-Andrés, I. Mártil, and G. González-Díaz, J. Appl. Phys. **107**, 103524 (2010).
[8]E. García-Hemme, R. García-Hernansanz, J. Olea, D. Pastor, A. Del Prado, I. Mártil, and G. González-Díaz, Appl. Phys. Lett. **104**, 211105 (2014).
[9]J. P. Mailoa *et al.*, Nat. Commun. **5**, 3011 (2014).
[10]W. Yang, J. Mathews, and J. Williams, Mater. Sci. Semicond. Process **62**, 103 (2017).
[11]J. M. Warrender, Q. Hudspeth, G. Malladi, H. Efstathiadis, and J. Mathews, Appl. Phys. Lett. **109**, 231104 (2016).
[12]P. K. Chow, W. Yang, Q. Hudspeth, S. Q. Lim, J. S. Williams, and J. M. Warrender, J. Appl. Phys. **123**, 133101 (2018).
[13]A. Luque, A. Martí, E. Antolín, and C. Tablero, Physica B **382**, 320 (2006).
[14]J. J. Krich, B. I. Halperin, and A. Aspuru-Guzik, J. Appl. Phys. **112**, 013707 (2012).
[15]J. M. Warrender, Appl. Phys. Rev. **3**, 031104 (2016).
[16]J. Olea, A. Del Prado, D. Pastor, I. Mártil, and G. González-Díaz, J. Appl. Phys. **109**, 113541 (2011).
[17]D. Pastor, J. Olea, A. Muñoz-Martín, A. Climent-Font, I. Mártil, and G. González-Díaz, J. Appl. Phys. **112**, 113514 (2012).
[18]H. Castán, E. Pérez, H. García, S. Dueñas, L. Bailón, J. Olea, D. Pastor, E. García-Hemme, M. Irigoyen, and G. González-Díaz, J. Appl. Phys. **113**, 024104 (2013).
[19]E. Antolín, A. Martí, J. Olea, D. Pastor, G. González-Díaz, I. Mártil, and A. Luque, Appl. Phys. Lett. **94**, 042115 (2009).
[20]W. Yang, A. J. Akey, L. A. Smillie, J. P. Mailoa, B. C. Johnson, J. C. McCallum, D. Macdonald, T. Buonassisi, M. J. Aziz, and J. S. Williams, Phys. Rev. Mater. **1**, 074602 (2017).
[21]E. García-Hemme, R. García-Hernansanz, J. Olea, D. Pastor, A. Del Prado, I. Mártil, and G. González-Díaz, Appl. Phys. Lett. **103**, 032101 (2013).
[22]D. Recht, M. J. Smith, S. Charnvanichborikarn, J. T. Sullivan, M. T. Winkler, J. Mathews, J. M. Warrender, T. Buonassisi, J. S. Williams, and S. Gradečak *et al.*, J. Appl. Phys. **114**, 124903 (2013).
[23]J. M. Warrender, J. Mathews, D. Recht, M. Smith, S. Gradečak, and M. J. Aziz, J. Appl. Phys. **115**, 163516 (2014).
[24]X. Qiu, X. Yu, S. Yuan, Y. Gao, X. Liu, Y. Xu, and D. Yang, Adv. Opt. Mater. **6**, 1700638 (2018).
[25]W. Yang, "Characterising and understanding Au-hyperdoped Si for sub-band gap optical absorption," Ph.D. thesis (The Australian National University, 2018).

[26]S. Q. Lim, C. T.-K. Lew, P. K. Chow, J. M. Warrender, J. S. Williams, and B. C. Johnson, APL Mater. **8**, 061109 (2020).
[27]C. Wu, C. Crouch, L. Zhao, J. Carey, R. Younkin, J. Levinson, E. Mazur, R. Farrell, P. Gothoskar, and A. Karger, Appl. Phys. Lett. **78**, 1850 (2001).
[28]C. H. Crouch, J. Carey, M. Shen, E. Mazur, and F. Genin, Appl. Phys. A **79**, 1635 (2004).
[29]J. Mathews, A. J. Akey, D. Recht, G. Malladi, H. Efstathiadis, M. J. Aziz, and J. M. Warrender, Appl. Phys. Lett. **104**, 112102 (2014).
[30]F. Liu, M. Wang, Y. Berencén, S. Prucnal, M. Engler, R. Hübner, Y. Yuan, R. Heller, R. Böttger, and L. Rebohle *et al.*, Sci. Rep. **8**, 4164 (2018).
[31]A. J. Akey, J. Matthews, and J. M. Warrender, "Maximum Ti concentrations in Si quantified with atom probe tomography," J. Appl. Phys. (to be published, 2021).
[32]A. Cullis, N. Chew, H. Webber, and D. J. Smith, J. Cryst. Growth **68**, 624 (1984).
[33]B. C. Johnson, J. C. McCallum, and M. J. Aziz, in *Handbook of Crystal Growth* (Elsevier, 2015), pp. 317–363.
[34]I. J. Raaijmakers and K.-B. Kim, J. Appl. Phys. **67**, 6255 (1990).
[35]D. Auston, C. Surko, T. Venkatesan, R. Slusher, and J. A. Golovchenko, Appl. Phys. Lett. **33**, 437 (1978).
[36]D. Auston, J. Golovchenko, A. Simons, R. Slusher, P. Smith, C. Surko, and T. Venkatesan, AIP Conf. Proc. **50**, 11 (1979).
[37]R. C. Bird and J. S. Williams, *Ion Beams for Materials Analysis* (Elsevier, 1990).
[38]L. R. Doolittle, Nucl. Instrum. Methods Phys. Res. B **9**, 344 (1985).
[39]S. Coffa, J. Poate, D. Jacobson, W. Frank, and W. Gustin, Phys. Rev. B **45**, 8355 (1992).
[40]J. Poate, D. Jacobson, J. Williams, R. Elliman, and D. Boerma, Nucl. Instrum. Methods Phys. Res. B **19**, 480 (1987).
[41]J. M. Poate, *Laser Annealing of Semiconductors* (Elsevier, 1982).
[42]F. Stevie, *Secondary Ion Mass Spectrometry: Applications for Depth Profiling and Surface Characterization* (Momentum Press, 2015).
[43]A. J. Akey, D. Recht, J. S. Williams, M. J. Aziz, and T. Buonassisi, Adv. Funct. Mater. **25**, 4642 (2015).
[44]A. A. Nikolskaya, D. S. Korolev, A. N. Mikhaylov, A. I. Belov, A. A. Sushkov, N. O. Krivulin, K. R. Muhamatchin, A. A. Elizarova, M. O. Marychev, and A. A. Konakov *et al.*, Appl. Phys. Lett. **113**, 182103 (2018).
[45]E. García-Hemme, R. García-Hernansanz, J. Olea, D. Pastor, A. Del Prado, I. Mártil, and G. Gonzalez-Diaz, Appl. Phys. Lett. **101**, 192101 (2012).
[46]It has been shown that the <111> orientation traps more solute than the <100> orientation,[58] However, <111> Si typically results in stacking faults during epitaxial growth.[33,59] Thus, we attribute the different qualities of epitaxy observed between the different experiments to the specific substrate orientation used.
[47]For the same laser wavelength and pulse duration, the observed behavior following PLM has a small dependence on laser fluence, as long as the fluence is sufficient to completely melt through the amorphous layer to the underlying crystal.
[48]F. Priolo, J. Poate, D. Jacobson, J. Batstone, J. Custer, and M. O. Thompson, Appl. Phys. Lett. **53**, 2486 (1988).
[49]J. Narayan, J. Cryst. Growth **59**, 583 (1982).
[50]K. Sánchez, I. Aguilera, P. Palacios, and P. Wahnón, Phys. Rev. B **79**, 165203 (2009).
[51]V. Markevich, S. Leonard, A. Peaker, B. Hamilton, A. Marinopoulos, and J. Coutinho, Appl. Phys. Lett. **104**, 152105 (2014).
[52]Interestingly, in the case of Si–Au, even with a substitutional Au concentration $N_{Au} > 10^{21}$ cm^{-3}, only a fraction of these Au atoms were opto-electrically active (<20%).[60]
[53]<100> has a higher interface velocity amorphization threshold than <111> Si.[32] Thus, more homogeneous Ti trapping is expected in <100> Si following PLM (i.e., good quality epitaxy and without breakdown), and consequently a higher D_b value for the same implant conditions.
[54]A. Hiraki, E. Lugujjo, and J. W. Mayer, J. Appl. Phys. **43**, 3643 (1972).
[55]G. Leclerc, L. Paquin, and F. Baratay, J. Mater. Res. **7**, 2458 (1992).
[56]S. Q. Lim, C. T.-K. Lew, P. K. Chow, J. M. Warrender, J. S. Williams, and B. C. Johnson, J. Appl. Phys. **126**, 224502 (2019).
[57]A. Cullis, H. Webber, J. Poate, and A. Simons, Appl. Phys. Lett. **36**, 320 (1980).
[58]D. E. Hoglund, M. O. Thompson, and M. J. Aziz, Phys. Rev. B **58**, 189 (1998).
[59]A. G. Cullis, H. C. Webber, N. G. Chew, J. M. Poate, and P. Baeri, Phys. Rev. Lett. **49**, 219 (1982).
[60]W. Yang, Q. Hudspeth, P. K. Chow, J. M. Warrender, N. Ferdous, E. Ertekin, G. Malladi, A. J. Akey, M. J. Aziz, and J. S. Williams, Phys. Rev. Applied **12**, 024015 (2019).